Search for Coherent Elastic Scattering of Solar ^{8}B Neutrinos in the XENON1T Dark Matter Experiment

E. Aprile,[1] J. Aalbers,[2] F. Agostini,[3] S. Ahmed Maouloud,[4] M. Alfonsi,[5] L. Althueser,[6] F. D. Amaro,[7] S. Andaloro,[8]
V. C. Antochi,[2] E. Angelino,[9] J. R. Angevaare,[10] F. Arneodo,[11] L. Baudis,[12] B. Bauermeister,[2] L. Bellagamba,[3]
M. L. Benabderrahmane,[11] A. Brown,[12] E. Brown,[13] S. Bruenner,[10] G. Bruno,[11] R. Budnik,[14, *] C. Capelli,[12]
J. M. R. Cardoso,[7] D. Cichon,[15] B. Cimmino,[16] M. Clark,[17] D. Coderre,[18] A. P. Colijn,[10, †] J. Conrad,[2]
J. Cuenca,[19] J. P. Cussonneau,[20] M. P. Decowski,[10] A. Depoian,[17] P. Di Gangi,[3] A. Di Giovanni,[11] R. Di Stefano,[16]
S. Diglio,[20] A. Elykov,[18] A. D. Ferella,[21, 22] W. Fulgione,[9, 22] P. Gaemers,[10] R. Gaior,[4] M. Galloway,[12] F. Gao,[23, 1, ‡]
L. Grandi,[24] C. Hils,[5] K. Hiraide,[25] L. Hoetzsch,[15] J. Howlett,[1, §] M. Iacovacci,[16] Y. Itow,[26] F. Joerg,[15] N. Kato,[25]
S. Kazama,[26, ¶] M. Kobayashi,[1] G. Koltman,[14] A. Kopec,[17] H. Landsman,[14] R. F. Lang,[17] L. Levinson,[14] S. Liang,[8]
S. Lindemann,[18] M. Lindner,[15] F. Lombardi,[7] J. Long,[24] J. A. M. Lopes,[7, ‖] Y. Ma,[27] C. Macolino,[28] J. Mahlstedt,[2]
A. Mancuso,[3] L. Manenti,[11] A. Manfredini,[12] F. Marignetti,[16] T. Marrodán Undagoitia,[15] K. Martens,[25]
J. Masbou,[20] D. Masson,[18] S. Mastroianni,[16] M. Messina,[22] K. Miuchi,[29] K. Mizukoshi,[29] A. Molinario,[22]
K. Morå,[1] S. Moriyama,[25] Y. Mosbacher,[14] M. Murra,[6] J. Naganoma,[22] K. Ni,[27] U. Oberlack,[5] K. Odgers,[13]
J. Palacio,[15, 20] B. Pelssers,[2] R. Peres,[12] M. Pierre,[20] J. Pienaar,[24] V. Pizzella,[15] G. Plante,[1] J. Qi,[27] J. Qin,[17]
D. Ramírez García,[18] S. Reichard,[19] A. Rocchetti,[18] N. Rupp,[15] J. M. F. dos Santos,[7] G. Sartorelli,[3] J. Schreiner,[15]
D. Schulte,[6] H. Schulze Eißing,[6] M. Schumann,[18] L. Scotto Lavina,[4] M. Selvi,[3] F. Semeria,[3] P. Shagin,[8]
E. Shockley,[27, 24] M. Silva,[7] H. Simgen,[15] A. Takeda,[25] C. Therreau,[20] D. Thers,[20] F. Toschi,[18] G. Trinchero,[9]
C. Tunnell,[8] K. Valerius,[19] M. Vargas,[6] G. Volta,[12] Y. Wei,[27] C. Weinheimer,[6] M. Weiss,[14] D. Wenz,[5] C. Wittweg,[6]
T. Wolf,[15] Z. Xu,[1] M. Yamashita,[26] J. Ye,[1, 27] G. Zavattini,[3, **] Y. Zhang,[1] T. Zhu,[1, ††] and J. P. Zopounidis[4]

(XENON Collaboration)[‡‡]

[1]*Physics Department, Columbia University, New York, NY 10027, USA*
[2]*Oskar Klein Centre, Department of Physics, Stockholm University, AlbaNova, Stockholm SE-10691, Sweden*
[3]*Department of Physics and Astronomy, University of Bologna and INFN-Bologna, 40126 Bologna, Italy*
[4]*LPNHE, Sorbonne Université, Université de Paris, CNRS/IN2P3, Paris, France*
[5]*Institut für Physik & Exzellenzcluster PRISMA, Johannes Gutenberg-Universität Mainz, 55099 Mainz, Germany*
[6]*Institut für Kernphysik, Westfälische Wilhelms-Universität Münster, 48149 Münster, Germany*
[7]*LIBPhys, Department of Physics, University of Coimbra, 3004-516 Coimbra, Portugal*
[8]*Department of Physics and Astronomy, Rice University, Houston, TX 77005, USA*
[9]*INAF-Astrophysical Observatory of Torino, Department of Physics,*
University of Torino and INFN-Torino, 10125 Torino, Italy
[10]*Nikhef and the University of Amsterdam, Science Park, 1098XG Amsterdam, Netherlands*
[11]*New York University Abu Dhabi, Abu Dhabi, United Arab Emirates*
[12]*Physik-Institut, University of Zürich, 8057 Zürich, Switzerland*
[13]*Department of Physics, Applied Physics and Astronomy, Rensselaer Polytechnic Institute, Troy, NY 12180, USA*
[14]*Department of Particle Physics and Astrophysics, Weizmann Institute of Science, Rehovot 7610001, Israel*
[15]*Max-Planck-Institut für Kernphysik, 69117 Heidelberg, Germany*
[16]*Department of Physics "Ettore Pancini", University of Napoli and INFN-Napoli, 80126 Napoli, Italy*
[17]*Department of Physics and Astronomy, Purdue University, West Lafayette, IN 47907, USA*
[18]*Physikalisches Institut, Universität Freiburg, 79104 Freiburg, Germany*
[19]*Institute for Astroparticle Physics, Karlsruhe Institute of Technology, 76021 Karlsruhe, Germany*
[20]*SUBATECH, IMT Atlantique, CNRS/IN2P3, Université de Nantes, Nantes 44307, France*
[21]*Department of Physics and Chemistry, University of L'Aquila, 67100 L'Aquila, Italy*
[22]*INFN-Laboratori Nazionali del Gran Sasso and Gran Sasso Science Institute, 67100 L'Aquila, Italy*
[23]*Department of Physics & Center for High Energy Physics, Tsinghua University, Beijing 100084, China*
[24]*Department of Physics & Kavli Institute for Cosmological Physics, University of Chicago, Chicago, IL 60637, USA*
[25]*Kamioka Observatory, Institute for Cosmic Ray Research, and Kavli Institute for the Physics and Mathematics*
of the Universe (WPI), the University of Tokyo, Higashi-Mozumi, Kamioka, Hida, Gifu 506-1205, Japan
[26]*Kobayashi-Maskawa Institute for the Origin of Particles and the Universe, and Institute for Space-Earth*
Environmental Research, Nagoya University, Furo-cho, Chikusa-ku, Nagoya, Aichi 464-8602, Japan
[27]*Department of Physics, University of California San Diego, La Jolla, CA 92093, USA*
[28]*Université Paris-Saclay, CNRS/IN2P3, IJCLab, 91405 Orsay, France*
[29]*Department of Physics, Kobe University, Kobe, Hyogo 657-8501, Japan*
(Dated: July 8, 2021)

We report on a search for nuclear recoil signals from solar ^{8}B neutrinos elastically scattering off
xenon nuclei in XENON1T data, lowering the energy threshold from 2.6 keV to 1.6 keV. We develop

a variety of novel techniques to limit the resulting increase in backgrounds near the threshold. No significant ^{8}B neutrino-like excess is found in an exposure of $0.6\,\mathrm{t} \times \mathrm{y}$. For the first time, we use the non-detection of solar neutrinos to constrain the light yield from 1-2 keV nuclear recoils in liquid xenon, as well as non-standard neutrino-quark interactions. Finally, we improve upon world-leading constraints on dark matter-nucleus interactions for dark matter masses between $3\,\mathrm{GeV}\,c^{-2}$ and $11\,\mathrm{GeV}\,c^{-2}$ by as much as an order of magnitude.

Introduction — Neutrinos from the Sun, atmospheric cosmic-ray showers, and supernovae can produce observable nuclear recoils (NRs) via coherent elastic scattering off nuclei in liquid xenon (LXe) detectors searching for dark matter (DM) [1]. The coherent elastic neutrino-nucleus scattering (CEνNS) process [2–5] produces the same signature as the one expected from DM-nucleus interactions, and thus the two can only be distinguished by their recoil spectra. Solar ^{8}B neutrinos are expected to contribute the greatest number of CEνNS events in LXe DM search experiments. These events fall near the energy thresholds of such detectors, with a spectrum indistinguishable from $6\,\mathrm{GeV}\,c^{-2}$ DM.

The XENON1T dark matter search experiment, operated at the INFN Laboratori Nazionali del Gran Sasso (LNGS) until Dec. 2018, used a sensitive target of 2.0 t of LXe in a two-phase time projection chamber (TPC). Two arrays of photomultiplier tubes (PMTs) at the top and bottom of the TPC allowed simultaneous detection of scintillation light (S1) and, via electroluminescence, ionization electrons (S2) [6, 7]. With the largest exposure of any LXe TPC, data from XENON1T has been used to search for a variety of DM candidates, resulting in world-leading upper limits for DM-nucleus interactions [8–11]. Though no excess of CEνNS from ^{8}B neutrinos (^{8}B CEνNS) was observed due to the energy threshold in these analyses, they will soon become an important background given the large exposures of next-generation multi-ton LXe detectors [12–14]. In this Letter, we present a search for ^{8}B CEνNS events in XENON1T data between Feb. 2, 2017 and Feb. 8, 2018 ("SR1" in Ref. [8]). In this new analysis, we achieve unprecedented sensitivity by reducing the energy threshold.

Analysis Strategy — The ^{8}B CEνNS expectation in XENON1T depends on: the ^{8}B neutrino flux Φ, measured [15, 16] as $(5.25 \pm 0.20) \times 10^6\,\mathrm{cm}^{-2}\,\mathrm{s}^{-1}$; the CE$\nu$NS cross section, from the Standard Model; the nuclear recoil scintillation light yield in xenon L_y; and the ionization yield Q_y. We first present a search for ^{8}B CEνNS events in XENON1T, expecting 2.1 CEνNS events given nominal estimates of the above variables. We then combine XENON1T data with external measurements, as appropriate, to constrain these variables. We constrain L_y by considering external measurements of Q_y and Φ. Next, by including external measurements of Q_y and L_y, we use XENON1T data to determine Φ independently. We also constrain non-standard neutrino interactions by relaxing the standard model assumption on the CEνNS cross section. Finally, by considering

^{8}B CEνNS as a background and applying external constraints on all variables, we use the data to set limits on DM-nucleus interactions.

CEνNS signal — The expected recoil spectrum of ^{8}B CEνNS in LXe is shown in Fig. 1 (top, dotted red). The scintillation and ionization responses are relatively uncertain at ^{8}B CEνNS energies ($< 2\,\mathrm{keV}$), and NR calibration measurements in XENON1T scarcely overlap this region, instead producing S1s and S2s similar to DM of mass $\geq 30\,\mathrm{GeV}\,c^{-2}$. Therefore, we modify the NR model in [8, 17] by decoupling the light and charge yields to allow for additional freedom.

The NR charge yield Q_y has been measured down to $0.3\,\mathrm{keV}$ [18], providing strong constraints at ^{8}B CEνNS energies which are included in v2.1.0 of the NEST package [19]. We use the best fit and uncertainty from NEST to define the shape of Q_y, fitting a single free "interpolation parameter" q to the measurements which specifies Q_y within this uncertainty, resulting in the model shown in Fig. 1 (middle). The central black line (edges of the shaded interval) in the figure corresponds to q equaling 0 (± 1). Measurements of the LXe NR light yield L_y [20] have a large ($\approx 20\,\%$) uncertainty near $1\,\mathrm{keV}$. Since the NEST L_y uncertainty is largely set by measurements at energies far above our region of interest (ROI), we fit these measurements using a free parameter that scales the NEST best fit L_y. These measurement and the resulting model are shown in Fig. 1 (bottom). The L_y and Q_y parameter fits use external measurements between 0.9 and $1.9\,\mathrm{keV}$, a central interval containing $68\,\%$ of expected ^{8}B CEνNS events after all acceptance losses. We conservatively assume zero L_y below $0.5\,\mathrm{keV}$, the lowest energy measurement available [21]. This treatment has a percent-level effect on the expected CEνNS rate, since the detection efficiency below this "cutoff energy" is $< 10^{-3}$.

The XENON1T S1 detection threshold was previously limited by the requirement that three or more PMTs detect pulses above threshold (denoted as "hits") within $50\,\mathrm{ns}$ [23], leading to a 1% acceptance of CEνNS recoils above the $0.5\,\mathrm{keV}$ cutoff. We reduce this "tight-coincidence" requirement to two hits within $50\,\mathrm{ns}$, increasing the total acceptance above the $0.5\,\mathrm{keV}$ cutoff to $5\,\%$. Another efficiency loss comes from ^{8}B CEνNS S2s failing the software trigger, which requires 60 significant PMT signals [24], or the S2 analysis threshold. The sensitivity is therefore impaired by the presence of electronegative impurities in the LXe, which reduce S2s along the drift path. The 120 PE S2 analysis threshold, re-
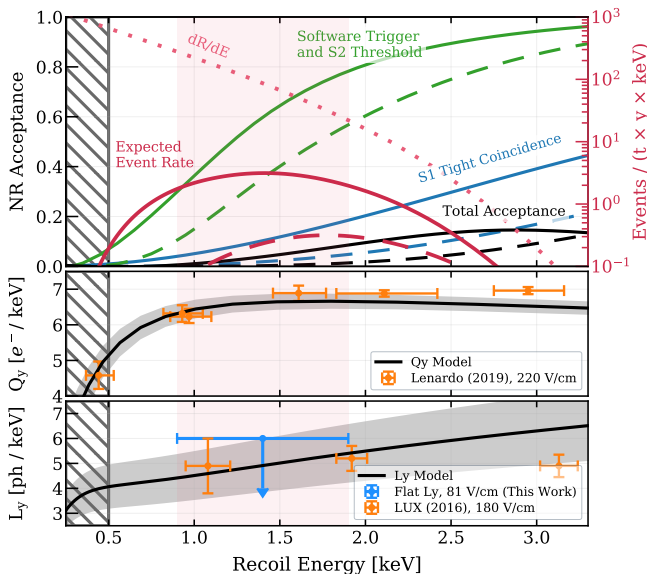
FIG. 1. Top: Improvement of the NR acceptance in this work (solid) with respect to previous DM analyses (dashed) [8, 22], including S1 detection efficiency (blue), software trigger and S2 threshold acceptance (green), and total acceptance after other quality and background rejection cuts (black). The right axis shows the recoil spectrum of ^{8}B CEνNS or dark matter of mass $6\,\mathrm{GeV}\,c^{-2}$ and cross section $4 \times 10^{-45}\,\mathrm{cm}^2$ (dotted pink), and the products of this spectrum with the total acceptances (red) as a function of true recoil energy. The acceptances and resulting spectra are based on the nominal (NEST) yield models. The red shaded interval contains 68 % of expected CEνNS events. Middle: The most precise available measurements of Q_y [18] (orange), with the Q_y model described in the text overlaid (black). Bottom: Constraints on L_y (in photons per keV) from LUX (orange) [20], and the 68 % upper limit from this work described in the Results section (blue), with the L_y model described in the text overlaid (black). To be conservative, no response is assumed below the $0.5\,\mathrm{keV}$ cutoff (hatched gray).

duced from 200 PE, accepts 92 % of CEνNS events that pass the software trigger. Acceptance losses due to new event selection criteria introduced to ress backgrounds are described below. Fig. 1 (top) shows the S1 tight-coincidence acceptances, software trigger and S2 threshold acceptances, and total acceptances for this and previous analyses, and the resulting spectra of expected ^{8}B CEνNS events. The Supplemental Material of this Letter provides details on the waveform simulation used to calculate all acceptances, and demonstrates excellent matching between real and simulated S1s and S2s. The overall change in acceptance results in a lowering of the energy threshold, defined as the energy where 5 % of recoils are detected, from $2.6\,\mathrm{keV}$ to $1.6\,\mathrm{keV}$. The ROI for the CEνNS search is defined by S2s between 120 and 500 photoelectrons (PE), and S1s between 1.0 and 6.0 PE consisting of two or three hits. In this ROI, the ^{8}B CEνNS signal expectation increases twentyfold with

respect to previous NR searches [8, 10, 11] because of the relaxed tight-coincidence requirement and lower S2 threshold, derived from integrating the expected event rate in Fig. 1 (top). Because of the minimal overlap with previously studied data, we consider this a blind analysis.

Backgrounds — This analysis considers all backgrounds described in [8, 17]. Radon daughters decaying on the inner surface of the TPC wall produce events with reduced S2s, contributing to the background in the ROI. In order to reduce this background to a negligible level, we use a fiducial volume of $1.04\,\mathrm{t}$, similar to the one chosen for [22] but smaller than the one used in [8].

The accidental coincidence (AC) of S1 and S2 peaks incorrectly paired by the XENON1T reconstruction software mimics real interactions. AC background events are modeled by sampling (with replacement) from isolated S1s and S2s and assigning a random time separation between them. Most S1s contributing to AC events originate from the pileup of lone hits from individual PMTs. Other sources include low-energy events occurring below the cathode or on the inner detector surface, and light leaking inside the active volume. AC forms the dominant background for this search, since the overall rate of isolated S1s increases by two orders of magnitude when we require only two hits. The rate and distribution of isolated S1s are determined using S1 peaks found in the extended event window of $1\,\mathrm{ms}$ before the S1 of high-energy events, as in [8, 17]. For this analysis, the data is reprocessed with an updated algorithm [25] to better retain the isolated S1s preceding these high-energy events, eliminating the dominant systematic uncertainty in the AC rate [8].

High-energy events from gamma-ray backgrounds can also contaminate subsequent events with lone hits, a dominant source of S1s in this analysis. For each event, the preceding event with the highest potential to produce lone hits is identified by dividing its largest S2 area by its time difference from the current event, denoted as $S2_{\mathrm{prev}}/\Delta t_{\mathrm{prev}}$. The selection $S2_{\mathrm{prev}}/\Delta t_{\mathrm{prev}} < 12\,\mathrm{PE}\,\mu\mathrm{s}^{-1}$ reduces the rate of isolated S1s by 65 %, accepting 87 % of ^{8}B CEνNS signals. Furthermore, we require the PMT signal sum within the first $1\,\mathrm{ms}$ of an event to be $< 40\,\mathrm{PE}$ and that this interval contains at most a single S1, accepting 96 % of remaining events. After these selections, the total isolated-S1 rate is $11.2\,\mathrm{Hz}$, ten times higher than for a threefold tight-coincidence requirement [8]. The total exposure after these selection criteria is $0.6\,\mathrm{t} \times \mathrm{y}$.

The same high-energy events can also produce small S2s appearing in subsequent events [26], potentially leading to unaccounted-for correlations between the isolated-S1 and isolated-S2 samples. In order to reduce these correlations, we further require that no S2 signal is found within the first millisecond of the event, and apply a cut on the horizontal spatial distance between the current and previous S2. These selections, together with the selection on $S2_{\mathrm{prev}}/\Delta t_{\mathrm{prev}}$, allow us to model the
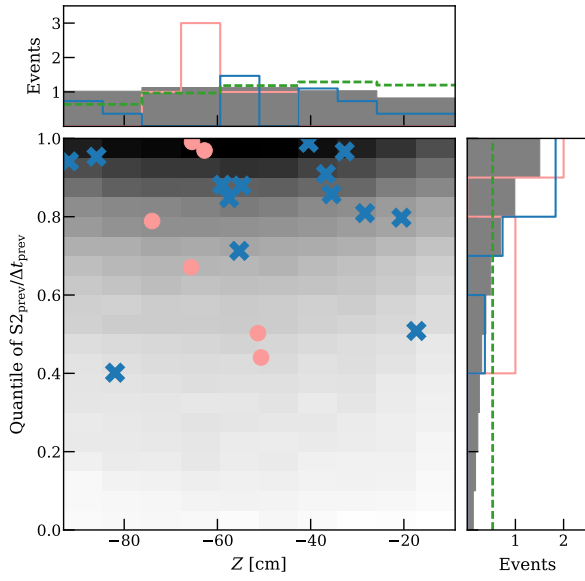
FIG. 2. Events in the science dataset (pink circles) and the AC-enriched validation region (blue crosses) projected onto Z and the quantile of the $S2_{prev}/\Delta t_{prev}$ value for NR signals. The AC model is shown in gray. Smaller panels show the projection of the model and data onto each axis, as well as the ^{8}B CEνNS model (green dashed), normalized to its upper limit. The AC-enriched region data in blue has a slightly different Z distribution due to the inverted GBDT cut, but is included for illustration, scaled by 0.36, the ratio of expected AC events in each dataset.

AC background for S2s down to 80 PE and reduce the isolated-S2 event rate therein to 1.0 mHz. For comparison, the isolated-S2 event rate in [8] was 2.6 mHz for S2s above 100 PE [8].

Selections that require both S1 and S2, such as the fiducial volume and S2 signal width [23] cuts (which depend on the interaction depth Z), are next applied to the combined synthetic AC events. Interactions on the TPC electrodes and in the xenon gas above the liquid surface contribute significantly to the isolated-S2 event rate, motivating a selection in a high-dimensional feature space as in [9]. In this analysis, a gradient boosted decision tree (GBDT) [27] ensemble is trained using the scikit-learn package [28] to optimize the signal and AC background discrimination based on the S2 area, the S2 rise time, the fraction of S2 area on the top array of PMTs, and Z. The GBDT selection reduces the AC background by 70 % while accepting ≥ 85 % of ^{8}B CEνNS events.

A background control region with S2 $<$ 120 PE contains $>$ 50 % of the AC background, and is excluded from the search for ^{8}B CEνNS due to its low detection probability. After closer inspection of the candidate waveforms in the control region, four events whose S1s contain more than one hit in the same channel, possibly due to afterpulsing of the PMTs [7], were removed. Twenty-three events remain, consistent with the AC background pre-

diction of 27.7 ± 1.4 events in the control region. Though the methods above yield a ≤ 5 % uncertainty on the AC background, we conservatively use an uncertainty of 20 % in the analysis to reflect the statistical uncertainty from the control region, but find that the CEνNS search is not strongly dependent on the uncertainty value within this range. Fig. 2 shows the AC model, events failing the GBDT cut, and science data projected onto Z and quantiles of $S2_{prev}/\Delta t_{prev}$.

Neutrons originating from radio-impurities inside detector materials produce NRs in the TPC, but the tight ROI reduces these to $0.039^{+0.002}_{-0.004}$ events. To limit the electronic recoil (ER) background dominated by β decays of ^{214}Pb (a daughter of ^{222}Rn), we additionally require $cS2_b$, the S2 area in the bottom array after a position-dependent correction [8], to be $<$ 250 PE. This reduces the ER background to 0.21 ± 0.08 events in the ROI, leading to a 4.2 % absolute acceptance loss for CEνNS. The same simulation procedure described in [17] is used to assess the neutron and ER backgrounds, as well as the associated uncertainties. The selection on $cS2_b$ has negligible effect on the AC background.

In the interpretation of the data, we utilize several features that differ between true S1-S2 events and AC. Lone hits are spread uniformly across the top and bottom PMT arrays, whereas scintillation light from the LXe volume mostly falls on the bottom array. Furthermore, an S1 with more than 2 PE on one PMT is very unlikely to be part of an AC, since most lone hits in XENON1T consist of a single photoelectron. We split the data into six "hit categories" according to the number and arrangement of S1 hits, and the largest hit-area (LHA), listed in Tab. I.

Inference — We analyze the data with a statistical model adapted from [17], with three continuous analysis dimensions; S2, Z, and the quantiles of equal signal acceptance in $S2_{prev}/\Delta t_{prev}$. The likelihood for XENON1T is the product of the likelihoods for each hit category, indexed with i:

$$\mathcal{L}_{Xe1T}(\Phi, Q_y, L_y, \vec{\theta}) = \prod_{i=1}^{6} \mathcal{L}_i(\Phi, Q_y, L_y, \vec{\theta}) \times \\ \prod_m [\mathcal{L}_m(\theta_m)]. \tag{1}$$

Here, $\vec{\theta}$ are the nuisance parameters. The extended unbinned likelihood terms $\mathcal{L}_i(\Phi, Q_y, L_y, \vec{\theta})$ are of the same form as Eq. (20) in [17], and include models in S2, Z and $S2_{prev}/\Delta t_{prev}$ for the ^{8}B CEνNS signal and AC, ER, and neutron backgrounds. The background component rates θ_m are constrained by the external measurement terms $\mathcal{L}_m(\theta_m)$.

For the ^{8}B CEνNS search, the nuisance parameters are the expectation values of the backgrounds, each with a constraint term, as well as the NR response parameters Q_y and L_y. The total likelihood used in the CEνNS

S1 hit properties		Science Data					AC validation region	
Hit Category	LHA	AC	ER	Total BG	CEνNS	Data	Expected	Data
2 Hits, 1+ in TA	$\geq$ 2PE	0.09	0.01	0.10	0.13	0	0.25	0
	< 2PE	3.54	0.04	3.58	0.44	4	9.45	10
2 Hits, 0 in TA	$\geq$ 2PE	0.03	0.03	0.06	0.23	0	0.11	0
	< 2PE	1.47	0.09	1.58	0.79	2	4.07	4
3 Hits	$\geq$ 2PE	0.00	0.01	0.02	0.17	0	0.03	0
	< 2PE	0.01	0.03	0.05	0.36	0	0.09	0
Total		5.14	0.21	5.38	2.11	6	14.00	14

TABLE I. Signal and background expectation values and observed event counts in six S1 hit classes based on number of S1 PMT hits in total, the number in the top array (TA), and the largest hit-area (LHA). Expectation values are computed for the nominal (NEST best fit) Q_y, L_y, and ^{8}B neutrino flux for the $0.6\,\mathrm{t} \times \mathrm{y}$ exposure. The neutron background is not shown separately in the table as it is significantly smaller than AC and ER, but is included in the background total. The last two columns show the result from the AC validation region, where the expectation value is dominated (97 %) by AC events, with the remainder from the expected ^{8}B CEνNS leakage. The relative uncertainties on the background and signal expectations are described in the text.

search is the product of $\mathcal{L}_{\mathrm{Xe1T}}$, defined in Eq. 1, and external constraints on Q_y and L_y, as detailed above. For these results, the models of CEνNS, DM, and the neutron background change both in shape and expectation value with Q_y and L_y. The CEνNS discovery significance as well as DM upper limits are computed using the log-likelihood-ratio test statistic calibrated with toy Monte-Carlo (toy-MC) simulations [17, 29].

To construct confidence intervals in Φ, Q_y, and L_y, we define a test statistic from the sum of profiled log-likelihoods of XENON1T and external constraints. By including external measurements of Q_y, we can constrain L_y. Since the CEνNS signal spans a narrow energy range, we use a constant L_y value to construct the intervals. This allows us to make use of the degeneracy between Φ and the NR response parameters Q_y and L_y, all three of which primarily affect the CEνNS expectation value. Details on the construction of these confidence intervals may be found in the Supplemental Material.

By including external constraints on Φ, Q_y, and L_y, this analysis can be used to consider physics processes beyond the Standard Model. We consider a benchmark model in which non-standard neutrino interactions modify the CEνNS cross section [3, 30, 31]. Our confidence interval on Φ assuming the Standard Model cross section can be reinterpreted as a confidence interval on the modified CEνNS cross section if we use the externally measured value of Φ. We also consider DM-nucleus interactions, including CEνNS as a background contribution, and Q_y and L_y as nuisance parameters. We use the same profile construction approach to compute upper limits as [17], including a power constraint [32].

Results — We estimated the probability of observing a 3σ (2σ) CEνNS excess in this data to be 20 % (50 %) for the nominal (NEST) values of Q_y, L_y. Inverting the GBDT cut gave an AC-rich validation region that was unblinded first (Tab. I). Background-only goodness-of-fit (GOF) tests using a binned Poisson likelihood were performed on the validation region, both for the six S1 hit categories and in the continuous analysis space, with p-values of 0.95 and 0.33, respectively, which exceeded the 0.05 validation criterion. The science dataset was unblinded following the successful validation region unblinding. Six events were found, as listed in Tab. I. The events are compatible with the background-only hypothesis, with a CEνNS discovery significance of $p > 0.50$. The same GOF tests used to assess the validation region unblinding show good agreement, with $p = 0.64$ and $p = 0.72$, respectively. The XENON1T confidence interval in Φ, Q_y, and L_y does not strongly constrain any of the parameters due to the significant correlation in particular between Φ and L_y, as shown by the green shaded region in Fig. 3 (top). On the other hand, Φ can be constrained if the external constraints on Q_y and L_y are included, as shown in the pink region, with a 90 % upper limit on Φ of $1.4 \times 10^7\,\mathrm{cm}^{-2}\mathrm{s}^{-1}$. The blue region in Fig. 3 shows the confidence interval from a combination of the XENON1T likelihood, constraints on Φ [16], and on Q_y. The 90 % upper limit on L_y (assumed constant over the $0.9 - 1.9$ keV energy range) is 9.4 ph/keV.

In the benchmark model of non-standard neutrino interactions considered, the electron neutrino has vector couplings to the up (u) and down (d) quarks of ε_{ee}^{dV} and ε_{ee}^{uV}, respectively [3, 30, 31]. The 90 % confidence interval for ε_{ee}^{dV} and ε_{ee}^{uV} from XENON1T data is shown in light blue in Fig. 4 (top).

The result for a spin-independent DM-nucleus interaction is shown in Fig. 4 (bottom). This constraint improves on previous world-leading limits [8, 9] in the mass range between $3\,\mathrm{GeV}\,c^{-2}$ and $11\,\mathrm{GeV}\,c^{-2}$ by as much as an order of magnitude. The limit lies at roughly the 15th percentile, reflecting the downwards fluctuation with respect to the background model (including CEνNS), but is not extreme enough to be power-constrained.

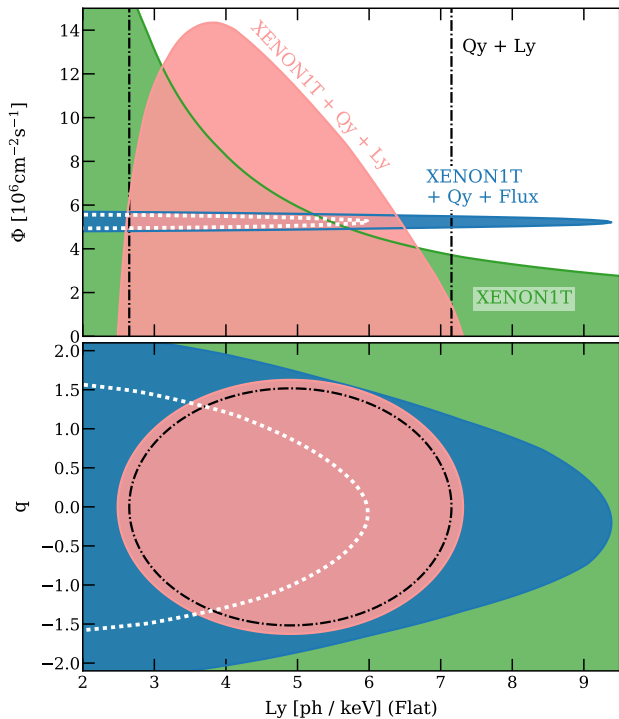*Outlook* — The XENONnT experiment, currently being commissioned at LNGS, aims to acquire a $20\,\mathrm{t} \times \mathrm{y}$

FIG. 3. Projections of the 90 % confidence volumes in L_y and Φ (top), and in L_y and the Q_y interpolation parameter q (bottom). The green area shows constraints using only the XENON1T data. Combining the XENON1T data and external constraints on Q_y [18] and L_y [21, 33] (shown in black dash-dotted lines) gives the confidence interval shown in pink, and an upper limit on Φ. Conversely, combining the XENON1T data and constraints on Φ [16] and Q_y yields the dark blue interval and upper limits on L_y. The dashed white line displays the 68 % confidence interval. L_y is assumed constant in the ^{8}B CEνNS ROI for these constraints.
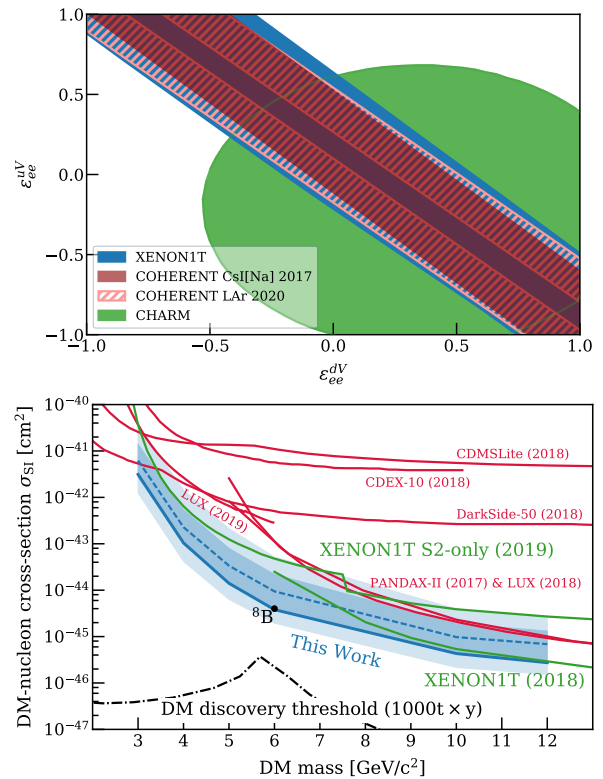

FIG. 4. Constraints on new physics using XENON1T data. Top: Constraints on non-standard vector couplings between the electron neutrino and quarks, where the XENON1T 90 % confidence interval (light blue region) is compared with the results from COHERENT [3, 30] (pink and dark red regions) and CHARM [34] (green). Bottom: The 90 % upper limit (blue line) on the spin-independent DM-nucleon cross section σ_{SI} as function of DM mass. Dark and light blue areas show the 1σ and 2σ sensitivity bands, and the dashed line the median sensitivity. Green lines show other XENON1T limits on σ_{SI} using the threefold tight-coincidence requirement [8] and an analysis using only the ionization signal [9], and other constraints [35–40] are shown in red. The dash-dotted line shows where the probability of a 3σ DM discovery is 90 % for an idealized, extremely low-threshold (3 eV) xenon detector with a $1000\,\mathrm{t} \times \mathrm{y}$ exposure [41]. The black dot denotes DM that has a recoil spectrum and rate identical to the ^{8}B neutrinos.

exposure [14]. As the isolated-S1 rate scales up with the larger number of PMTs and the isolated-S2 rate with the detector surface area, the AC background will be the biggest challenge for the discovery of ^{8}B CEνNS. The AC background modeling and discrimination techniques used in this analysis will improve the sensitivity of XENON1T to ^{8}B CEνNS and low-mass DM. The novel cryogenic liquid circulation system developed to ensure efficient purification in XENONnT will mitigate the reduction of S2s due to impurities, improving the acceptance of low-energy NRs from ^{8}B neutrinos and DM. Additionally, the data will be analyzed in a triggerless mode to minimize efficiency loss and better understand the AC background. Together with the significantly larger exposure, these techniques give XENONnT strong potential to discover ^{8}B CEνNS.

The large uncertainty in both Q_y and L_y will be the dominant systematic in constraining new physics from DM and non-standard neutrino interactions. Improving these uncertainties by calibrating NRs in LXe using *in*

situ low energy neutron sources [42] and dedicated detectors [18] can crucially improve the sensitivity of next-generation experiments to both ^{8}B CEνNS and light DM.

---

[*] Also at Simons Center for Geometry and Physics and C. N. Yang Institute for Theoretical Physics, SUNY, Stony Brook, NY, USA

[†] Also at Institute for Subatomic Physics, Utrecht University, Utrecht, Netherlands

[‡] feigao@tsinghua.edu.cn

[§] joseph.howlett@columbia.edu

[¶] Also at Institute for Advanced Research, Nagoya University, Nagoya, Aichi 464-8601, Japan

[‖] Also at Coimbra Polytechnic - ISEC, Coimbra, Portugal

[**] Also at INFN, Sez. di Ferrara and Dip. di Fisica e Scienze della Terra, Università di Ferrara, via G. Saragat 1, Edificio C, I-44122 Ferrara (FE), Italy

[††] tianyu.zhu@columbia.edu

[‡‡] xenon@lngs.infn.it

[1] J. Billard, L. Strigari, and E. Figueroa-Feliciano, Implication of neutrino backgrounds on the reach of next generation dark matter direct detection experiments, Phys. Rev. D **89**, 023524 (2014), arXiv:1307.5458 [hep-ph].

[2] D. Z. Freedman, Coherent effects of a weak neutral current, Phys. Rev. D **9**, 1389 (1974).

[3] D. Akimov et al. (COHERENT Collaboration), Observation of coherent elastic neutrino-nucleus scattering, Science **357**, 1123 (2017), arXiv:1708.01294.

[4] H. Bonet et al., Constraints on Elastic Neutrino Nucleus Scattering in the Fully Coherent Regime from the CONUS Experiment, Phys. Rev. Lett. **126**, 041804 (2021), arXiv:2011.00210 [hep-ex].

[5] A. Aguilar-Arevalo et al. (CONNIE Collaboration), Exploring low-energy neutrino physics with the Coherent Neutrino Nucleus Interaction Experiment, Phys. Rev. D **100**, 092005 (2019), arXiv:1906.02200 [hep-ex].

[6] Aprile, E. et al. (XENON Collaboration), The XENON1T dark matter experiment, Eur. Phys. J. C **77**, 881 (2017), arXiv:1708.07051.

[7] E. Aprile et al. (XENON Collaboration), Lowering the radioactivity of the photomultiplier tubes for the XENON1T dark matter experiment, Eur. Phys. J. C **75**, 546 (2015), arXiv:1503.07698 [astro-ph.IM].

[8] E. Aprile et al. (XENON Collaboration), Dark matter search results from a one ton-year exposure of XENON1T, Phys. Rev. Lett. **121**, 111302 (2018), arXiv:1805.12562.

[9] E. Aprile et al. (XENON Collaboration), Light Dark Matter Search with Ionization Signals in XENON1T, Phys. Rev. Lett. **123**, 251801 (2019), arXiv:1907.11485 [hep-ex].

[10] E. Aprile et al. (XENON Collaboration), Constraining the spin-dependent WIMP-nucleon cross sections with XENON1T, Phys. Rev. Lett. **122**, 141301 (2019), arXiv:1902.03234.

[11] E. Aprile and et al. (XENON Collaboration), First Results on the Scalar WIMP-Pion Coupling, Using the XENON1T Experiment, Phys. Rev. Lett. **122**, 071301 (2019), arXiv:1811.12482.

[12] H. Zhang et al. (PandaX Collaboration), Dark matter direct search sensitivity of the PandaX-4T experiment, Sci. China Phys. Mech. Astron. **62**, 31011 (2019).

[13] D. Akerib et al. (LUX-ZEPLIN Collaboration), Projected wimp sensitivity of the LUX-ZEPLIN dark matter experiment, Phys. Rev. D **101**, 052002 (2020).

[14] E. Aprile et al. (XENON Collaboration), Projected WIMP Sensitivity of the XENONnT Dark Matter Experiment, J. Cosmol. Astropart. Phys. **11** (2020), 031, arXiv:2007.08796.

[15] M. Agostini et al. (Borexino Collaboration), Comprehensive measurement of pp-chain solar neutrinos, Nature **562**, 505 (2018).

[16] B. Aharmim et al. (SNO Collaboration), Combined Analysis of all Three Phases of Solar Neutrino Data from the Sudbury Neutrino Observatory, Phys. Rev. **C88**, 025501 (2013), arXiv:1109.0763 [nucl-ex].

[17] E. Aprile et al. (XENON Collaboration), XENON1T dark matter data analysis: Signal and background models and statistical inference, Phys. Rev. D **99**, 112009 (2019), arXiv:1902.11297 [physics.ins-det].

[18] B. Lenardo et al., Low-Energy Physics Reach of Xenon Detectors for Nuclear-Recoil-Based Dark Matter and Neutrino Experiments, Phys. Rev. Lett. **123**, 231106 (2019), arXiv:1908.00518.

[19] M. Szydagis et al., Noble Element Simulation Technique, 10.5281/zenodo.3905382 (2018), v2.1.0 (uncertainties from private communication).

[20] D. Akerib et al. (LUX Collaboration), Low-energy (0.7-74 kev) nuclear recoil calibration of the lux dark matter experiment using d-d neutron scattering kinematics (2016), arXiv:1608.05381 [physics.ins-det].

[21] D. Huang, Ultra-Low Energy Calibration of the LUX and LZ Dark Matter Detectors, Ph.D. thesis, Brown U. (2020).

[22] E. Aprile et al. (XENON Collaboration), First Dark Matter Search Results from the XENON1T Experiment, Phys. Rev. Lett. **119**, 181301 (2017), arXiv:1705.06655 [astro-ph.CO].

[23] E. Aprile et al. (XENON Collaboration), XENON1T Dark Matter Data Analysis: Signal Reconstruction, Calibration and Event Selection, Phys. Rev. D **100**, 052014 (2019), arXiv:1906.04717 [physics.ins-det].

[24] E. Aprile et al. (XENON Collaboration), The XENON1T data acquisition system, JINST **14** (07), P07016, arXiv:1906.00819.

[25] XENON Collaboration, The pax data processor v6.11.1, 10.5281/zenodo.4290785 (2020).

[26] D. S. Akerib et al. (LUX Collaboration), Investigation of background electron emission in the LUX detector (2020), arXiv:2004.07791 [physics.ins-det].

[27] J. H. Friedman, Greedy function approximation: a gradient boosting machine, Annals of statistics **29**, 1189 (2001).

[28] F. Pedregosa *et al.*, Scikit-learn: Machine learning in Python, Journal of Machine Learning Research **12**, 2825 (2011).

[29] C. Patrignani *et al.* (Particle Data Group), Review of Particle Physics, Chin. Phys. **C40**, 100001 (2016).

[30] D. Akimov *et al.* (COHERENT Collaboration), First Measurement of Coherent Elastic Neutrino-Nucleus Scattering on Argon, Phys. Rev. Lett. **126**, 012002 (2021), arXiv:2003.10630 [nucl-ex].

[31] S. Brice *et al.*, A method for measuring coherent elastic neutrino-nucleus scattering at a far off-axis high-energy neutrino beam target, Phys. Rev. D **89**, 072004 (2014), arXiv:1311.5958 [physics.ins-det].

[32] G. Cowan, K. Cranmer, E. Gross, and O. Vitells, Power-Constrained Limits, arXiv:1105.3166 [physics.data-an] (2011).

[33] D. S. Akerib *et al.* (LUX Collaboration), Low-energy (0.7-74 kev) nuclear recoil calibration of the LUX dark matter experiment using d-d neutron scattering kinematics (2016), arXiv:1608.05381 [physics.ins-det].

[34] J. Dorenbosch *et al.* (CHARM Collaboration), Experimental Verification of the Universality of ν_e and ν_μ Coupling to the Neutral Weak Current, Phys. . B **180**, 303 (1986).

[35] R. Agnese *et al.* (SuperCDMS Collaboration), Low-mass dark matter search with CDMSlite, Phys. Rev. D **97**, 022002 (2018), arXiv:1707.01632 [astro-ph.CO].

[36] H. Jiang *et al.* (CDEX Collaboration), Limits on light weakly interacting massive particles from the first 102.8 kg × day data of the cdex-10 experiment, Phys. Rev. Lett. **120**, 241301 (2018).

[37] P. Agnes *et al.* (DarkSide Collaboration), DarkSide-50 532-day dark matter search with low-radioactivity , Phys. Rev. D **98**, 102006 (2018), arXiv:1802.07198 [astro-ph.CO].

[38] D. S. Akerib *et al.* (LUX Collaboration), Results from a Search for Dark Matter in the Complete LUX Exposure, Phys. Rev. Lett. **118**, 021303 (2017), arXiv:1608.07648 [astro-ph.CO].

[39] X. Cui *et al.* (PandaX-II Collaboration), Dark Matter Results from 54-Ton-Day Exposure of PandaX-II Experiment, Phys. Rev. Lett. **119**, 181302 (2017), arXiv:1708.06917 [astro-ph.CO].

[40] D. Akerib *et al.* (LUX), Extending light WIMP searches to single scintillation photons in LUX, Phys. Rev. D **101**, 042001 (2020), arXiv:1907.06272 [astro-ph.CO].

[41] F. Ruppin, J. Billard, E. Figueroa-Feliciano, and L. Strigari, Complementarity of dark matter detectors in light of the neutrino background, Phys. Rev. D **90**, 083510 (2014), arXiv:1408.3581 [hep-ph].

[42] J. I. Collar, Applications of an ^{88}Y/Be photoneutron calibration source to dark matter and neutrino experiments, Phys. Rev. Lett. **110**, 211101 (2013).

[43] L. Wolfenstein, Neutrino Oscillations in Matter, Phys. Rev. D **17**, 2369 (1978).

[44] A. Friedland, C. Lunardini, and C. Pena-Garay, Solar neutrinos as probes of neutrino matter interactions, Phys. Lett. B **594**, 347 (2004), arXiv:hep-ph/0402266.

[45] F. Capozzi, E. Di Valentino, E. Lisi, A. Marrone, A. Melchiorri, and A. Palazzo, Global constraints on absolute neutrino masses and their ordering, Phys. Rev. D **95**, 096014 (2017), [Addendum: Phys.Rev.D 101, 116013 (2020)], arXiv:2003.08511 [hep-ph].

SUPPLEMENTAL MATERIAL

Waveform Simulation

The S1 and S2 detection efficiencies in the CEνNS ROI cannot easily be measured with a calibration source. Therefore, we use a waveform simulation, which produces PMT waveforms in the CEνNS ROI, to calculate those efficiencies.

Some of the S1s detected by two or more PMTs do not meet the requirement that hits on those PMTs occur within 50 ns. The fraction of the S1s passing this tight-coincidence requirement thus correlates with the S1 width. We use an exponential function to describe the distribution of photons detected by PMTs in the simulation to facilitate tuning of the S1 width. The S1 time distribution is independent of the number of hits in XENON1T data. This allows us to calibrate the exponential function by matching simulated S1s to those in data.

Four more detector effects are included in the simulation: the probability that the PMT photocathode emits two photoelectrons when absorbing one photon, the electronic noise level, the single photoelectron spectrum of the PMTs, and PMT after-pulses. The full simulation process establishes the relation between the number of detected photons and the size of the S1 and S2 [17].

The mean and spread of the S1 width distribution vary with the size of the S1. Simulated waveforms and XENON1T data are processed with the same software. The S1 width parameter in the simulation is tuned to minimize the chi-square between simulated and observed mean width as shown in Fig. 5.

The software trigger efficiency of the S2 varies with its size and the position of the event. Events from the deeper part of the detector produce wider S2s, and have a lower trigger efficiency. Specifically, in waveform simulation, we use effective models to reproduce the diffusion, size, and temporal distribution of ionization signals. Together with the four detector effects mentioned above, the simulation output is compared to background S2s originating on the detector wall in both width and triggered fraction, since wall events have a smaller S2 size due to charge loss on surfaces. The excellent matching between simulated and wall events, shown in Fig. 5 and Fig. 6, validates the response of the detector to small S2s.

Signal expectation

From the standard solar model, the energy of solar ^{8}B neutrinos is below ~ 20 MeV, giving a maximum momentum transfer $q_{max} \sim 40$ MeV, much smaller than the Z boson mass [1]. Under this condition, the Standard Model predicts that the tree-level differential CEνNS
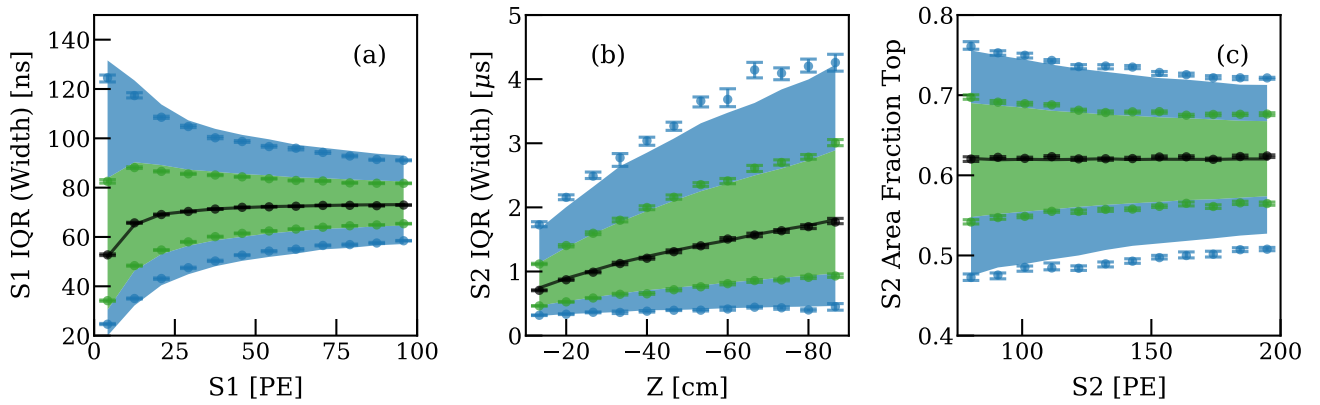
FIG. 5. Matching of the S1 and S2 properties of the waveform simulation and detector data originating from the TPC wall. The plots show (a) the interquartile range (IQR), the range of time covering the central 50 % area, as a function of S1 size, (b) IQR of S2 < 200 PE as a function of depth (Z), and (c) the fraction of signal detected by the top PMT array in each S2 ($-10\,\text{cm} < Z < 90\,\text{cm}$). The dots denote quantiles of the detector data, corresponding to $\pm\,2\,\sigma$ (blue), $\pm\,1\,\sigma$ (green), and median (black). Colored bands show the same quantiles with the simulation data. Both detector and simulation data are events close to the wall, with the same position, S1 size, and S2 size distributions.
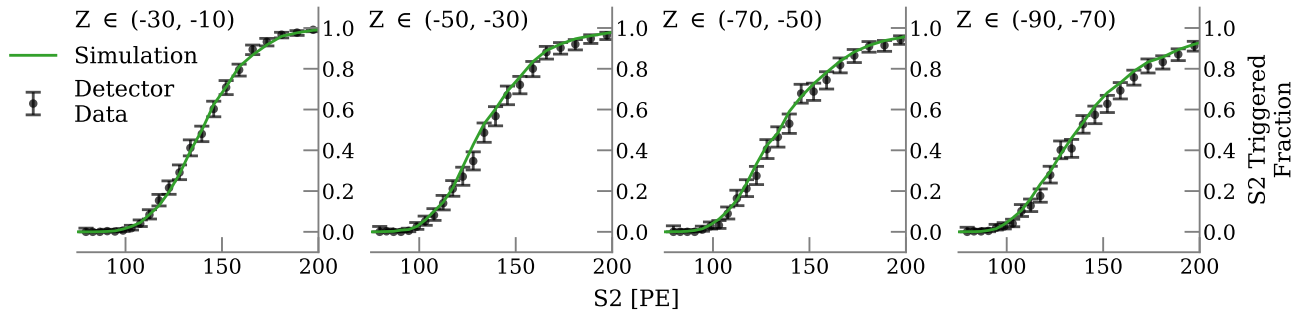

FIG. 6. Efficiencies (fraction of S2 passed) of the software trigger as a function of the S2 size at different depth (Z) ranges (in cm) show agreement between the simulation and detector data. The black dots correspond to the events in detector data, that were triggered by their S1. The green line shows the fraction of simulated S2 passing the trigger, produced with the same position distribution as the S1-triggered detector data.

cross section is given by:

$$\frac{\mathrm{d}\sigma_{\mathrm{CE}\nu\mathrm{NS}}}{\mathrm{d}E_r} = \frac{G_F^2}{4\pi} Q_w^2 M \left(1 - \frac{M E_r}{2 E_\nu^2}\right) F(E_r)^2, \quad (2)$$

where E_r is the NR energy, G_F is the Fermi constant, M is the target nuclear mass of the recoiling atom, E_ν is the incoming neutrino energy, $F(E_r)$ is the nuclear form factor, and Q_w is the nuclear weak charge [2]. Here, we have neglected the contribution from the hadronic axial-vector current, because the spin-dependent structure factors are negligible compared with spin-independent structure factors for xenon [10]. Since $M \gg E_\nu \gg E_r$, terms of higher order in E_r/E_ν are dropped as well.

We also consider a non-standard interaction following [30, 31], where the weak charge in electron neutrino scattering is replaced by $Q_w \to \widetilde{Q}_w = N(1 + 2\varepsilon_{ee}^{uV} + 4\varepsilon_{ee}^{dV}) + Z(4\sin^2\theta_w - 1 + 4\varepsilon_{ee}^{uV} + 2\varepsilon_{ee}^{dV})$, with two non-standard couplings ε_{ee}^{uV} and ε_{ee}^{dV}. Neutrino oscillation must be included, since our model assumes that only electron

neutrinos have non-zero non-standard interactions. In the energy range of solar ⁸B neutrinos, their oscillation to other flavors through interactions with matter in the Sun (the MSW effect) is important [43]. In the standard model, this effect can be interpreted as an equivalent index of refraction $n = 1 + \sqrt{2} G_F N_e / E_\nu$ for electron neutrinos, with N_e being the electron number density. Our model assumes two additional non-standard interactions ε_{ee}^{uV} and ε_{ee}^{dV}, so the index of refraction should be modified to be $\widetilde{n} = 1 + \sqrt{2} G_F (N_e + \varepsilon_{ee}^{uV} N_u + \varepsilon_{ee}^{dV} N_d)/E_\nu$, where N_u (N_d) is the number density of up (down) quarks. Thus, the inclusion of non-standard interactions also makes the survival probability of electron neutrinos P_e epsilon-dependent [44]. The neutrino oscillation parameters in the following calculation are from [45]. Using $\Phi = (5.25 \pm 0.20) \times 10^6\,\text{cm}^{-2}\text{s}^{-1}$ and letting $\eta(E_r)$ be the NR acceptance, the final expected CEνNS rate

from solar ^{8}B neutrinos is

$$R(\varepsilon_{ee}^{uV}, \varepsilon_{ee}^{dV}) = \frac{1}{M} \int \frac{d\sigma}{dE_r} \frac{d\Phi}{dE_\nu} \eta(E_r) \, dE_\nu dE_r, \qquad (3)$$

where $d\sigma/dE_r$ is given by

$$\frac{d\sigma}{dE_r} = \frac{d\sigma_{\text{CE}\nu\text{NS}}}{dE_r} \frac{\widetilde{Q}_w^2}{Q_w^2} P_e + \frac{d\sigma_{\text{CE}\nu\text{NS}}}{dE_r}(1 - P_e). \qquad (4)$$

So the upper limit on Φ can be converted into ε_{ee}^{uV}-ε_{ee}^{dV} space by solving:

$$\left\langle R(\varepsilon_{ee}^{uV}, \varepsilon_{ee}^{dV}) \right\rangle < \frac{\Phi_{\text{limit}}}{\Phi} \left\langle R(\varepsilon_{ee}^{uV} = 0, \varepsilon_{ee}^{dV} = 0) \right\rangle, \qquad (5)$$

where $\langle \cdot \rangle$ denotes the isotopic average (assuming natural abundances in xenon), and $\Phi_{\text{limit}} = 1.4 \times 10^7 \text{ cm}^{-2}\text{s}^{-1}$ is the upper limit on Φ (see Results section).

More details on the AC background

The rates of isolated S1s and isolated S2s are significantly increased following high-energy events, mainly due to gamma-ray backgrounds. In XENON1T, we found that the rate of single-electron S2s and lone hits on PMTs are correlated with $S2_{\text{prev}}/\Delta t_{\text{prev}}$. Fig. 7 shows the distribution of $S2_{\text{prev}}/\Delta t_{\text{prev}}$ for both isolated S1s and high-energy events themselves. The distribution for high-energy events reflects that of signal events, since neither are correlated with preceding S2s. Thus, a selection requiring $S2_{\text{prev}}/\Delta t_{\text{prev}} \leq 12 \, \text{PE}/\mu\text{s}$ rejects 65% of isolated S1s (and consequently AC events) with 87% signal acceptance.

Although the selection on $S2_{\text{prev}}/\Delta t_{\text{prev}}$ also suppresses the rate of isolated S2s, those that remain near the 80 PE threshold are still correlated with $S2_{\text{prev}}/\Delta t_{\text{prev}}$. To remove this correlation, we utilize the horizontal (X,Y) positions of isolated S2s, calculated from fitting their PMT distribution patterns, similar to [23]. We investigate the horizontal spatial distance of isolated S2s from previous high energy events, $\sqrt{(X - X_{\text{prev}})^2 + (Y - Y_{\text{prev}})^2}$, to quantify the correlation between them, as shown in Fig. 8. A distinctive population with small $\sqrt{(X - X_{\text{prev}})^2 + (Y - Y_{\text{prev}})^2}$ values is seen near the 80 PE threshold. A cut, shown as a red line, rejects $> 99\%$ of events that occur at the same (X, Y) position as the preceding event but are reconstructed with non-zero mean-squared distance due to uncertainties in the reconstructed positions. The acceptance of this cut as a function of S2 is studied by randomly associating two uncorrelated events, and ranges from 92% at 120 PE to $> 99\%$ for S2 > 500 PE.

Details on constructing confidence volumes

Since the NR response uncertainty is large, the test statistic distribution for confidence intervals will depend
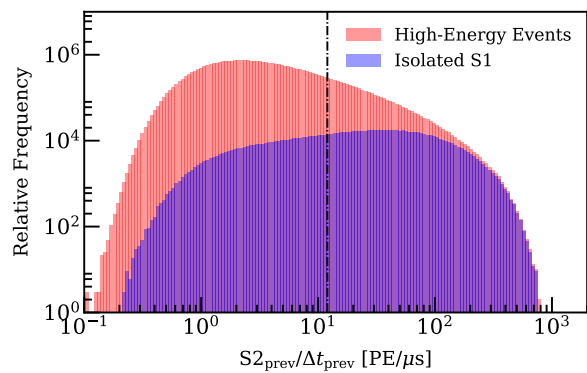

FIG. 7. Distribution in $S2_{\text{prev}}/\Delta t_{\text{prev}}$ space of both high-energy events and isolated S1s immediately preceding them. At large $S2_{\text{prev}}/\Delta t_{\text{prev}}$ values, a significant fraction of high energy events contain an isolated S1 before the trigger. The discrimination between signal events (which have the same distribution as high-energy events) and isolated S1s allows the selection $S2_{\text{prev}}/\Delta t_{\text{prev}} \leq 12\text{PE}/\mu\text{s}$, shown as a vertical black dash-dotted line, which rejects 65% of background with 87% signal acceptance.
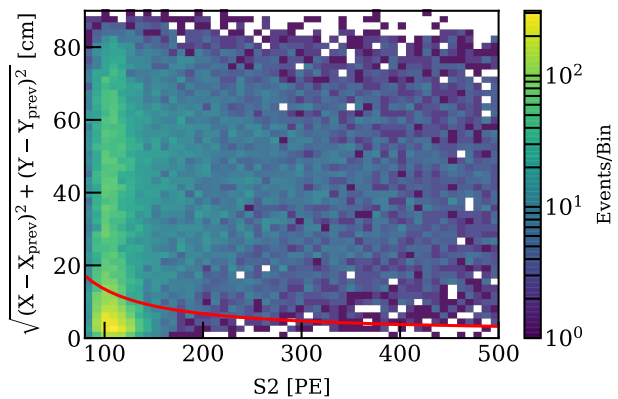

FIG. 8. Horizontal spatial distance of isolated S2s with respect to previous high-energy events. Events below the red line are removed to ensure no correlation between isolated S2s and the preceding high-energy event.

on the true values of Φ, Q_y, and L_y. To compute a unified confidence interval in all these parameters in the manner of [17] and the DM results in this paper, we would have to estimate the distribution of the test statistic using toy-MC computations in these three dimensions. However, the strong degeneracy between these parameters allows us to avoid this extensive computation. For the relevant range for this search, and the low number of events expected, the CEνNS model shape changes so little with Q_y and L_y that inference results are not affected: Computing the discovery significance of toy-MC simulations either fitting these shape parameters, fixing them to their true values or shifting them by $+2\sigma$

each yielded no discernible bias, and a spread compatible with toy-MC variation only. Therefore, only when computing confidence intervals on Φ[1], Q_y, and L_y, the CEνNS model shape is fixed, and these variables appear in the likelihood only via the expression for the expectation value of detected CEνNS events, $\mu_{CE\nu NS}(\Phi, Q_y, L_y)$. Therefore, we can compute the profile likelihood ratio and toy-MC estimates of the test statistic distribution in the space of $\mu_{CE\nu NS}$ alone. External constraints on Φ, L_y, and Q_y are implemented as terms λ_F, λ_{L_y}, and λ_{Q_y}, corresponding to the profiled log-likelihood-ratios for Gaussian measurements of each parameter. We combine the XENON1T profiled log-likelihood ratio $\lambda_{Xe1T}(\mu_{CE\nu NS}(\Phi, Q_y, L_y))$ and different combinations of

external constraints into test statistics Λ:

$$
\begin{aligned}
\Lambda_A(\Phi, Q_y, L_y) =& \lambda_{Xe1T}(\mu_{CE\nu NS}(\Phi, Q_y, L_y)) \\
\Lambda_B(\Phi, Q_y, L_y) =& \lambda_{Xe1T}(\mu_{CE\nu NS}(\Phi, Q_y, L_y)) + \\
& \lambda_{Q_y}(Q_y) + \lambda_{CE\nu NS}(\Phi) \\
\Lambda_C(\Phi, Q_y, L_y) =& \lambda_{Xe1T}(\mu_{CE\nu NS}(\Phi, Q_y, L_y)) + \\
& \lambda_{Q_y}(Q_y) + \lambda_{L_y}(L_y).
\end{aligned} \tag{6}
$$

For each Λ, the toy-MC results of $\lambda_{Xe1T}(\mu_{CE\nu NS})$ is combined with random realizations of the other profiled likelihoods in a grid of Φ, Q_y, and L_y to provide the 90th percentile of Λ for each point in parameter space, which is compared with $\Lambda(\Phi, Q_y, L_y)$ to construct confidence intervals. The test statistic Λ_A, shown in green in Fig. 3 in the main text, represents the confidence interval using the XENON1T data only. The strong anti-correlation between Φ and L_y is apparent in Fig. 3 (top). To compute a confidence interval on L_y, we include constraints on Q_y [18] and Φ [16] in Λ_B, shown in dark blue in Fig. 3 in the main text. Last, combining XENON1T, and constraints on Q_y [18] and L_y [21, 33] into Λ_C yields an upper limit on the CEνNS interaction rate Φ.

---

[1] Also used for the non-standard neutrino interaction result